

See discussions, stats, and author profiles for this publication at: <https://www.researchgate.net/publication/241690370>

Examination of the Factors Affecting the Electrochemical Performance of Oxygen-Terminated Polycrystalline Boron-Doped Diamond Electrodes

ARTICLE in ANALYTICAL CHEMISTRY · JUNE 2013

Impact Factor: 5.64 · DOI: 10.1021/ac401042t · Source: PubMed

CITATIONS

27

READS

143

6 AUTHORS, INCLUDING:



[Eleni Bitziou](#)

The University of Warwick

19 PUBLICATIONS 246 CITATIONS

SEE PROFILE



[Robert Barry Channon](#)

The University of Warwick

3 PUBLICATIONS 33 CITATIONS

SEE PROFILE



[Mark Edward Newton](#)

The University of Warwick

105 PUBLICATIONS 1,784 CITATIONS

SEE PROFILE



[Julie V Macpherson](#)

The University of Warwick

175 PUBLICATIONS 5,625 CITATIONS

SEE PROFILE

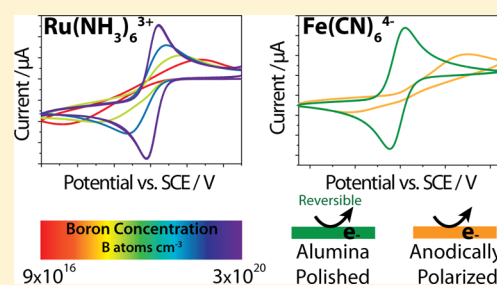
Examination of the Factors Affecting the Electrochemical Performance of Oxygen-Terminated Polycrystalline Boron-Doped Diamond Electrodes

Laura A. Hutton,[†] James G. Iacobini,[†] Eleni Bitziou,[†] Robert B. Channon,[†] Mark E. Newton,[‡] and Julie V. Macpherson^{*,†}

Departments of [†]Chemistry and [‡]Physics, University of Warwick, Coventry CV4 7AL, United Kingdom

S Supporting Information

ABSTRACT: In order to produce polycrystalline oxygen-terminated boron-doped diamond (BDD) electrodes suitable for electroanalysis (i.e., widest solvent window, lowest capacitive currents, stable and reproducible current responses, and capable of demonstrating fast electron transfer) for outer sphere redox couples, the following factors must be considered. The material must contain enough boron that the electrode shows metal-like conductivity; electrical measurements demonstrate that this is achieved at $[B] > 10^{20}$ B atoms cm^{-3} . Even though BDD contains a lower density of states than a metal, it is not necessary to use extreme doping levels to achieve fast heterogeneous electron transfer (HET). An average $[B] \sim 3 \times 10^{20}$ B atoms cm^{-3} was found to be optimal; increasing $[B]$ results in higher capacitive values and increases the likelihood of nondiamond carbon (NDC) incorporation. Hydrogen-termination causes a semiconducting BDD electrode to behave metal-like due to the additional surface conductivity hydrogen termination brings. Thus, unless $[B]$ of the material is known, the electrical properties of the electrode may be incorrectly interpreted. Note, this layer (formed on a lapped electrode) is electrochemically unstable, an effect which is exacerbated at increased potentials. It is essential during growth that NDC is minimized as it acts to increase capacitive currents and decrease the solvent window. We found complete removal of NDC after growth using aggressive acid cleans, acid cycling, and diamond polishing impossible. Although hydrogen termination can mask the NDC signature in the solvent window and lower capacitive currents, this is not a practical procedure for improving sensitivity in electroanalysis. Finally, alumina polishing of lapped, NDC free, freestanding, BDD electrodes was found to be an effective way to produce well-defined, stable, and reproducible surfaces, which support fast (reversible) HET for $\text{Fe}(\text{CN})_6^{4-}$ electrolysis, the first time this has been reported at an oxygen-terminated surface.



Carbon electrodes continue to be the subject of intensive investigation, given their importance in many fields ranging from sensors,¹ to fuel cell catalyst supports.² A significant body of research is dedicated to understanding how material properties control electrochemical characteristics for both inner and outer sphere redox couples, in order to optimize electrode performance.³ Boron-doped diamond (BDD) is an important member of the carbon electrode family, which is being employed increasingly in electrochemical applications.^{1b,4} In contrast to the vast majority of all other carbon electrodes, BDD is the only carbon electrode, in its purest form, which does not contain sp^2 carbon. This leads to extremely interesting electrochemical properties,⁵ such as the widest potential window of all carbon electrodes, low background currents, and an increased resistance to electrochemical fouling,^{1b,6} making it particularly attractive for use in electroanalysis.

Dependent on the growth conditions employed, both thin and thick films can be grown, where the grain size of the growth face typically increases with film thickness. During growth, it is also possible to vary the boron dopant density $[B]$ of the material and, hence, electrical properties, by controlling the

concentration of boron in the gas phase.⁷ At high $[B]$, it is easier to synthesize poly- (or nano-)crystalline material than single-crystal BDD.⁸ Hence, the vast majority of electrochemical applications focus on this material, which is typically synthesized using the chemical vapor deposition (CVD) method.

As crystallographic orientation influences the amount of boron taken up,⁹ poly- (or nano-)crystalline material has a boron content which varies heterogeneously. As for other carbon materials, such as carbon nanotubes, the growth conditions also determine the quality of the resulting material, in terms of the sp^2/sp^3 ratio.¹⁰ For BDD, sp^2 carbon, residing either at grain boundaries or within the grain itself, can affect electrochemical performance.

As CVD growth occurs in a hydrogen-rich atmosphere, the majority of studies tend to focus on hydrophobic hydrogen-terminated BDD electrodes, often referred to as, "as grown".¹¹

Received: April 9, 2013

Accepted: June 22, 2013

Published: June 22, 2013



Table 1. Material and Electrochemical Characteristics of pBDD Electrodes from Various Sources

electrode	source	diamond structure	[B] (boron atoms cm ⁻³)	resistivity (Ω cm)	sp ² signature	solvent window (V)	capacitance (μF cm ⁻²)
A (low, fs)	NRL	freestanding microcrystalline	9.2×10^{16}	40700	no	4.11	2.9 (±0.1)
B (low-mid, fs)	E6	freestanding microcrystalline	2×10^{18}	88	yes	3.89	8.5 (±0.5)
C (mid, fs)	NRL	freestanding microcrystalline	mid 10^{19*}	42	no	3.67	3.3 (±0.3)
D (high, fs)	E6	freestanding microcrystalline	1.9×10^{20}	0.06	yes	3.53	11 (±0.5)
E (high, fs)	E6	freestanding microcrystalline	3×10^{20} (av)	0.05	no	3.60	6.5 (±0.4)
			1.9×10^{20} (low)				
			4.7×10^{20} (high)				
F (high, thin) as-received	Condias	Nb substrate microcrystalline	1.9×10^{20}	—	yes	2.30	3.9 (±0.4)
O-term						1.43	23 (±0.5)
G (very high, thin) as-received	ADT	Nb substrate microcrystalline	1.6×10^{21}	—	yes	1.38	153 (±3)
O-term						—	381 (±8)

However, the hydrogen-terminated layer on intrinsic diamond, in the presence of water, is now known to support surface conductance.^{12,13} Furthermore, although the hydrogen-terminated surface is stable over many months in air, the surface can gradually oxidize.^{11c,14} In contrast, oxygen-termination does not result in a measurable surface conductivity.

In this paper, we explore the effect of [B], sp² carbon content, and different pretreatment processes on the electrochemical response of both inner and outer sphere electron transfer mediators at oxygen-terminated polycrystalline BDD (pBDD) electrodes. In this way, we provide a benchmark for other researchers wishing to work with oxygen-terminated pBDD electrodes with material properties which show fast heterogeneous electron transfer (HET: for outer sphere redox couples over a wide potential range), while maintaining as low as possible background signals with the widest extended solvent window characteristics. We also investigate and compare the electrochemical stability of lapped (~nm surface roughness) oxygen- and hydrogen-terminated pBDD electrodes over different electrochemical potential ranges.

EXPERIMENTAL SECTION

Solutions. All solutions were prepared from Milli-Q water (Millipore Corp.) with a resistivity of 18.2 MΩ cm at 25 °C. To test the electrochemical characteristics of the pBDD electrodes, solutions containing potassium hexachloroiridate(III) (IrCl₆³⁻, Sigma Aldrich Company), hexaamineruthenium(III) chloride [Ru(NH₃)₆³⁺, Strem Chemicals, Newbury Port, MA], ferrocenylmethyltrimethylammonium hexafluorophosphate (FcTMA⁺, made in-house), potassium ferrocyanide (Fe(CN)₆⁴⁻, Sigma Aldrich Company), and iron(II) sulfate (Fe²⁺, Sigma Aldrich Company) were employed, either in 0.1 M KNO₃ (Fischer Scientific) or perchloric acid (HClO₄, Sigma Aldrich Company). Sulfuric acid 99.999% (H₂SO₄; Sigma Aldrich Company) was used for anodic polarization.

pBDD Materials. Seven pBDD electrodes labeled A–G, from four different sources, with dopant densities in the range from 9.2×10^{16} to 1.6×10^{21} boron atoms cm⁻³ were utilized in this study and detailed in Table 1, along with material properties. The information in parentheses next to the electrode label (Table 1) denotes the level of boron content (low, mid, high, and very high) and whether the film is thin

(and supported on a substrate) or thick enough (>200 μm) to be freestanding (fs). The electrodes were sourced from the Naval Research Laboratory (NRL), Washington DC, USA (A and C); Element Six Ltd (E6), Ascot, U.K. (B, D and E); Condias GmbH, Itzehoe, Germany (F) and Advanced Diamond Technologies (ADT), Inc., Illinois, USA (G). Electrodes D–G are commercially available. Electrodes A–E are freestanding and have all been mechanically lapped (polished) prior to use, employing a resin-bonded scaife embedded with diamond grit particles between 2–20 μm in size. The scaife was rotated at 3000 rpm and the diamond electrodes were also rotated and translated while in contact with the wheel in order to ensure multidirectional polishing of the polycrystalline surface, resulting in ~nm surface roughness. In contrast, electrodes F and G are thin film (7 μm and 2 μm thick, respectively) and attached to a niobium substrate. Contact angle measurements revealed electrode F was predominantly hydrogen-terminated prior to use, whilst electrode G had suffered partial air oxidation.

Electrode Fabrication: Electrodes A to E (fs). A laser micromachiner (E-355H-3-ATHI-O system, Oxford Lasers) was used to cut 1 mm diameter pBDD columns from the diamond wafers provided, which were acid cleaned in boiling concentrated H₂SO₄ (98%), supersaturated with KNO₃.¹⁵ This process removed any nondiamond carbon (NDC) generated during laser micromachining¹⁶ and also served to oxygen-terminate the pBDD surface.¹⁷ A reliable ohmic connection¹⁸ was made to the back of the pBDD columns by sputtering (Edwards E606 sputter/evaporator) Ti (20 nm) | Au (1 μm) and then annealing in a tube oven in air at 400 °C for 4 h. A similar method to the standard procedure for producing glass-sealed microelectrodes¹⁹ was employed to insulate the pBDD columns so that only the top (disc) surface was exposed.¹⁵

Prior to use, the electrode was freshly cleaned using alumina polish (0.05 μm sized particles, micropolish, Buehler, Germany) on a distilled water saturated polishing pad (microcloth, Buehler). To ensure the complete removal of alumina particles, the electrode was then either polished using a dry, clean, microcloth polishing pad or placed in distilled water in a sonicator (Ultrasonic cleaner, VWR), for 60 s.²⁰ For some studies the electrode was deliberately subject to a strong anodic polarization (3 V vs SCE for 60 s in 0.1 M H₂SO₄).

Electrode Fabrication: Electrodes F and G (thin). To maintain sample integrity, thin film electrodes F and G were cleaned using a different procedure, described in section 1 of the Supporting Information. Electrical contact was made via an annealed Ti/Au contact to the underlying niobium substrate, with the top surface masked off using insulating Kapton tape (RS Components Ltd., Northants, U.K.), which contained a 1 mm diameter hole, cut via laser ablation, to define the electrode area. Electrochemical measurements were made on both as-received (no cleaning) and acid-cycled (potential cycling from -2 to 2 V in 0.1 M H_2SO_4 until reproducible CVs were achieved) surfaces.

Hydrogen Termination. Electrodes B (low-mid, fs) and E (high, fs) were hydrogen-terminated in a hydrogen plasma CVD reactor at 1 kW and 60 Torr for a period of 10 min (Department of Chemistry, University of Bristol, U.K.). The CVD reactor was powered down, while hydrogen was passed over the surface at a constant flow rate of 500 sccm. The electrodes were further left to cool under this hydrogen flow for 10 min. Contact angle measurements performed prior to electrochemistry showed the surfaces to be hydrophobic (i.e., hydrogen-terminated).²¹

Material Characterization Measurements. Secondary Ion Mass Spectrometry (SIMS). SIMS (Cameca IMS 4f) measurements to determine $[\text{B}]$ were carried out at the Loughborough Surface Analysis Centre. As the materials are polycrystalline, to obtain the average doping level, a large area spot (~ 0.16 mm²) was employed. For grain-dependent SIMS, a smaller spot (~ 0.05 mm²) was used. SIMS was calibrated by assuming that the boron signal was a linear function of the carbon signal over the concentration range from 1×10^{14} atoms cm⁻³ to 7×10^{21} atoms cm⁻³. A calibration standard was prepared by ion implantation of boron into single crystal diamond with a peak boron concentration of 1×10^{19} atoms cm⁻³ at a depth of 1 μm . A SIMS profile versus sample depth was used to generate the linear calibration factor for the given experimental conditions.

Raman. Micro-Raman was performed at room temperature with a Renishaw inVia Raman microscope. An excitation wavelength of 514.5 nm was employed using an Ar^+ laser with a power of 10 mW. A spot size of ca. 3 μm was used and detection was carried out with a CCD detector (visible to near IR).

Field Emission Scanning Electron Microscopy (FE-SEM). FE-SEM images were recorded using a high-resolution Zeiss Supra 55 VP. An in-lens detector was used at accelerating voltages between 2 and 15 kV with a working distance of 4 mm.

White Light Interferometry (WLI). WLI images were recorded using a WYKO Systems WLI: WYKO NT-2000 surface profiler.

Electrical Resistivity. The resistivity of electrodes A (low, fs) through E (high, fs) was measured with a source meter (Keithley Instruments Inc., Cleveland, Ohio) by applying a constant current of 10 μA and recording the resulting voltage/resistance at an ambient temperature of 23 $^\circ\text{C}$. A four point Van Der Pauw probe configuration was employed using annealed Ti/Au contacts, to negate possible contact resistance effects. Electrical contact to the diamond was made with micropositioning probes (Quarter Research and Development, Bend, Oregon) positioned on annealed Ti/Au pads, enabling ohmic connection to the BDD.

X-ray Photoelectron Spectroscopy (XPS). XPS was performed using an Omicron Sphera analyzer with an Omicron

XM1000 monochromated Al $K\alpha$ source (1486.6 eV energy) at a 30° takeoff angle, with a sampling size ca. 1.1 mm in diameter.

Electrochemical Measurements. All electrochemical measurements were made in a three-electrode mode using a potentiostat (CHI730A, CH Instruments, Inc. Austin, TX) connected to a laptop computer. A saturated calomel electrode (SCE) or a leak-free Ag/AgCl electrode were used as reference electrodes with a Pt gauze serving as a counter electrode. The laboratory was air conditioned to 23 ± 1 $^\circ\text{C}$ for all measurements.

RESULTS AND DISCUSSION

BDD Characterization. In order to explore the factors which affect the electrochemical response and stability of oxygen-terminated pBDD, seven different electrodes of defined area (1 mm diameter disk) from various sources spanning a range of diamond morphologies, boron content, and quality were investigated. Studies initially focused on freshly cleaned surfaces. Prior to electrochemical analysis, the material structure, electrical properties, and NDC carbon content were characterized using SIMS, resistivity measurements, FE-SEM, and micro-Raman (as detailed in the Experimental Section) and summarized in Table 1.

The electrodes fall into two main categories, freestanding microcrystalline pBDD films, electrodes A (low, fs) to E (high, fs) increasing in average $[\text{B}]$ from 9.2×10^{16} (A) to 3×10^{20} (E) (all >200 μm thick) and thin film microcrystalline pBDD on niobium substrates, electrodes F (high, thin) and G (very high, thin). Figure 1 shows the grain structure revealed by in-

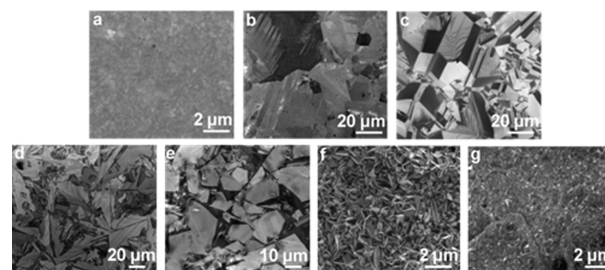


Figure 1. In-lens FE-SEM images of pBDD electrodes A–G (a–g, respectively).

lens secondary electron FE-SEM images for the seven pBDD electrodes. Electrodes A (low, fs) to E (high, fs) have all been lapped,²² to reveal a surface roughness of $<5 \pm 0.5$ nm rms, as determined by atomic force microscopy (AFM) (data not shown). The thinness of electrodes F (high, thin) and G (very high, thin) means they cannot be polished; they have as-grown surface rms roughnesses of 1.85 ± 0.4 μm and 9.3 ± 0.4 μm , respectively, determined by white-light interferometry (data not shown).

Of the freestanding electrodes, A (low, fs) is the thinnest at 210 μm and thus has the smallest grain size, ranging from 100 nm to 1 μm . In contrast, B (low-mid, fs) is the thickest at 880 μm with grain size from 7 to 100 μm , while C (mid, fs) is 380 μm thick with a grain size in the range from 2 to 25 μm . While the thickness of electrodes D (high, fs) and E (high, fs) are similar at ca. 635 μm and contain similar $[\text{B}]$ (Table 1), the randomly orientated grain structure is different (Figure 1, panels d and e). This is due to differences in the pressure, power density, and source carbon concentrations of the growth plasma, as well as the deposition temperature of the substrate.²³

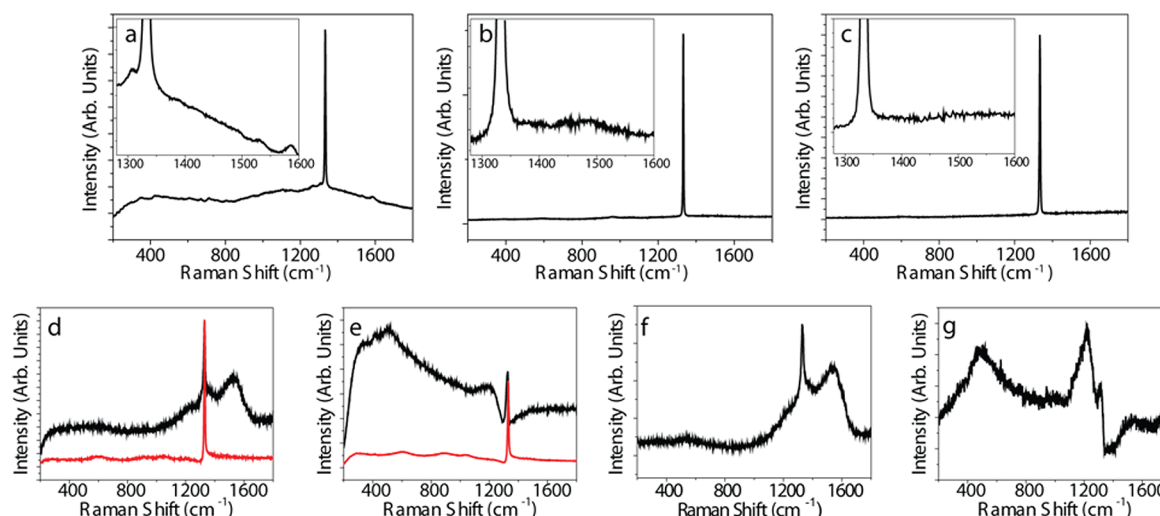


Figure 2. Typical Raman spectra for the seven pBDD electrodes A–G (a–g, respectively) recorded at room temperature with a 514.5 nm laser. The insets in spectra (a, b, and c) are zoom-ins of the sp^2 (NDC) region, and (d) and (e) show Raman spectra for the low-doped (red) and higher-doped (black) grains.

Previous FE-SEM work on pBDD material of a similar boron dopant density to electrodes D (high, fs) and E (high, fs) showed that the dark regions correlated with more highly boron-doped regions. By inference, this is also most likely true for electrodes B (low-mid, fs) and C (mid, fs).²⁴

Average [B] was determined by SIMS for each electrode, apart from C (mid, fs), which was previously reported to have an average [B] of mid 10^{19} boron atoms cm^{-3} .^{11a} For electrode E (high, fs), the grain size meant it was also possible to take SIMS measurements in both the high and lower-doped grains, showing a greater than $\times 2$ difference in [B] (Table 1). Electrical sheet resistivity measurements were only possible for the freestanding electrodes, as the thin film electrodes reside on a conducting support. Importantly, a clear trend of decreasing resistivity with increasing average [B] is observed (Table 1).^{7c} The resistivity and SIMS data indicate that electrodes D–F are just above the metallic threshold [D (high, fs) and F (high, thin) have the same doping level],^{7a,25} while A (low, fs) to C (mid, fs) are in the semiconducting region.^{7c,26} G (very high, thin) is doped (1.6×10^{21} boron atoms cm^{-3}) strongly into the metallic regime.

Micro-Raman spectroscopy was used to investigate the sp^3 – sp^2 content of the seven electrodes and also provide further qualitative information on [B]. Figure 2 shows typical micro-Raman spectra taken at a wavelength of 514.5 nm for electrodes A–G (a–g, respectively). All spectra are representative of many ($n = 7$) recorded in different locations. Figure 2 (panels d and e) contain two spectra as it was possible to interrogate both the high (black line)- and low (red line)-doped grains of electrodes D (high, fs) and E (high, fs). The diamond zone center optical phonon peak, attributed to sp^3 carbon bonding, is obvious in all spectra, occurring at 1332 cm^{-1} for electrodes A (low, fs) to C (mid, fs), whereas a shift to lower wavenumbers is observed for electrodes D (high, fs) to G (very high, thin), especially in the darker (FE-SEM) grains, consistent with higher [B].²⁷ Asymmetric deformation and attenuation of the sp^3 peak is also observed for electrodes D (high, fs) to G (very high, thin), a feature attributed to a Fano-type interference between the discrete zone center optical phonon and a continuum of electronic excitations, typically seen at $[\text{B}] > 10^{20}$ boron atoms cm^{-3} .²⁸ Broad features at ca. 500 and 1220 cm^{-1} are seen only

for electrodes D (high, fs) to G (very high, thin) and are more prominent in the higher-doped grains [D (high, fs) and E (high, fs)]. These peaks have also been reported in the literature for other BDD materials when [B] is in the range from 10^{20} to 10^{22} atoms cm^{-3} .²⁵

NDC, such as graphite and amorphous carbon, is typically seen in polycrystalline BDD between 1400 and 1600 cm^{-1} .²⁹ Within the resolution of micro-Raman, electrodes C (mid, fs) and E (high, fs) show no evidence of NDC, whereas electrodes B (low-mid, fs), D (high, fs), F (high, thin), and G (very high, thin) all show NDC features, as highlighted in the higher resolution inset of Figure 2b and Figure 2 (panels d, f, and g). NDC features are easier to see in spectra associated with the metallic electrodes D (high, fs), F (high, thin), and G (very high, thin) due to the attenuation of the sp^3 peak as a result of high boron uptake. The least-doped electrode A (low, fs) shows a high background, most likely due to luminescence, which can mask the presence of NDC.³⁰ Note, for electrodes A (low, fs), B (low-mid, fs), and D (high, fs), even after diamond polishing and stringent acid cleaning, NDC is still present. Interestingly, the NDC signal in electrode D (high, fs) appears only to be prominent in the higher-doped grains, as shown in Figure 2d and in Raman maps, reported in section 2 of the Supporting Information, where it is also clear that the NDC is prominent within the grain and not just at the boundaries. These higher-doped, lower-quality grains constitute less than half the surface (as determined from FE-SEM). In contrast, single point Raman measurements and Raman mapping of electrode E (high) shows no evidence of sp^2 content within any grain.

pBDD Background Electrochemical Processes. Solvent windows for electrodes A to G were recorded in 0.1 M KNO_3 ($\text{pH} = 6.5$) at a scan rate of 100 mV s^{-1} and compared against a commercially available 2 mm diameter Pt disk and 3 mm diameter glassy carbon (GC) disk electrode, as shown in Figure 3a, where the cyclic voltammograms (CVs) have been vertically offset for clarity. This is further emphasized in section 3 of the Supporting Information, where CVs of electrodes D (high, fs) and E (high, fs), along with Pt and GC, are plotted on the same graph. The electrochemical process of water decomposition (for a given pH) defines the solvent window, where hydrogen and oxygen evolution takes place at cathodic and anodic

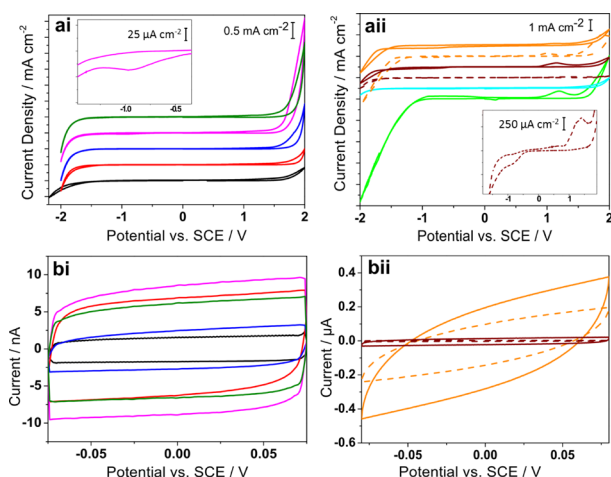


Figure 3. CVs in aerated 0.1 M KNO_3 recorded at a scan rate of 0.1 V s^{-1} over the potential range (a) -2 V to 2 V (where CVs have been vertically offset for clarity) and (b) -0.07 to 0.07 V vs SCE, for (i) 1 mm diameter freestanding electrodes A (black), B (red), C (blue), D (pink), and E (green) and (ii) thin film electrodes F (brown) and G (orange), as-grown (dashed) and acid-cycled (solid). Also shown is the response for platinum (light green) and glassy carbon (light blue). Note the difference in current density scales between (a) and (b) and also (bi) and (bii).

extremes, respectively. Here, we define the anodic and cathodic potential limits as the potential at which a current of 0.4 mA cm^{-2} is passed for water electrolysis, as documented in Table 1. For Pt and GC due to the high background processes ($>0.4 \text{ mA cm}^{-2}$) it was not possible to quote a solvent window using this definition.

For freestanding pBDD electrodes A (low, fs) to E (high, fs), two trends are apparent; first, all show wider potential windows than Pt and GC (Figure 3, panels ai and aii, Table 1 and section 3 of the Supporting Information). Second, as $[\text{B}]$ increases, the solvent window can be seen to decrease slightly (Table 1 and Figure 3ai).²⁹ Electrode A (low, fs), which contains the lowest $[\text{B}]$, and has the highest resistivity, exhibits the widest solvent window, especially in the cathodic region, due to the limited number of charge carriers, especially at negative potentials. To be efficient, water electrolysis requires the presence of catalytic sites on the electrode surface (inner sphere electron transfer).³¹ Water electrolysis is hindered at metallic pBDD electrodes, D (high, fs) and E (high, fs), compared to GC and Pt, most likely due to a lack of available binding sites on the oxygen-terminated surface to mediate heterogeneous electron transfer (HET).³² On Pt and GC, both unfilled d orbitals and reactive quininelike groups are present, respectively, enabling more efficient water-electrode interactions.³³ Interestingly, the presence of NDC in electrode D (high, fs) is not sufficient to significantly affect the width of the solvent window, as it shows a similar solvent window to negligible NDC electrode, E (high, fs). However, while the CVs for electrodes A (low, fs) to C (mid, fs) and E (high, fs) appear featureless between -1.5 V and $+1.5 \text{ V}$, electrode D (high, fs) does show evidence of a reduction peak between -0.7 and -0.95 V (Figure 3ai, inset), most likely due to NDC impurities, providing catalytic sites for oxygen reduction. Similar responses have been reported for pBDD electrodes which contain sp^2 carbon.^{11a,34}

For the thin film electrodes, as-grown electrode F (high, thin) shows a wider solvent window than G (very high, thin). Features are evident in the CV for electrode F at $+1.4 \text{ V}$ and

-0.95 V (Figure 3aii, inset), which increase significantly in magnitude and shift to more kinetically facile potentials of $+1.15 \text{ V}$ and -0.91 V , after potential cycling in acid due to the increased presence of oxygen containing redox-active NDC impurities.^{10c,35} This is also observed to a greater extent for electrode G. These processes were greater in magnitude for the first acid cycle, decreasing with subsequent cycles (data not shown) until a constant response was observed (data in Figure 3aii), indicative of a decrease in NDC content.^{11a,36} However, not all NDC was removed. Acid cycling was found to decrease the solvent window of both electrodes (Table 1).

From Raman, although the NDC content of electrode F (high, thin) appears similar to that of the highly doped grains in electrode D (high), the currents associated with NDC-driven electrochemical processes are almost a factor of 10 greater at electrode F. Although electrode F is rougher than D (roughness factor ~ 3.5), this is unlikely to account for the order of magnitude increase. Instead, we attribute the difference to the fact that over half the surface of electrode D contains lower-doped and, importantly, negligible NDC-containing grains. In contrast, no area of electrode F was found to be NDC-free on the scale of the micro-Raman measurement. Finally, for the highest-doped electrode (G), both as-received and oxygen terminated, the solvent window is not as wide as that for glassy carbon (Figure 3 aii).

Capacitance values, C , of $2.9 (\pm 0.1)$, $8.5 (\pm 0.5)$, $3.3 (\pm 0.3)$, $11 (\pm 0.5)$, and $6.5 (\pm 0.4) \mu\text{F cm}^{-2}$ were determined from the CV data presented in Figure 3bi for the pBDD electrodes A–E, respectively, at 0 V versus SCE in 0.1 M KNO_3 , using $C = i_{\text{average}} / \nu A_{\text{geometric}}$, where i_{average} is the current average from the forward and reverse sweep, ν is the scan rate, and $A_{\text{geometric}}$ the geometric electrode area. The measured values are all lower than that measured at the GC and Pt electrodes, $24 (\pm 2)$ and $35 (\pm 3) \mu\text{F cm}^{-2}$, respectively. This is likely to originate from the lower local density of states for pBDD compared to classical electrode materials³⁷ and a significant reduction in surface-driven redox processes, especially in the case of negligible NDC content. By comparing the capacitance values measured at the three NDC-free pBDD electrodes, A (low, fs), C (mid, fs), and E (high, fs), it can be seen that increasing boron content acts to increase the measured capacitance, most likely due to an increasing LDOS. On the basis of boron content alone, electrodes B (low-mid, fs) and D (high, fs) have higher capacitance values than expected. We attribute this to the presence of NDC.

Thin film electrode F (high, thin) gave significantly higher capacitance values after oxidation [$23 (\pm 0.5) \mu\text{F cm}^{-2}$] via acid cycling, as opposed to when as-grown (H-terminated: $3.9 (\pm 0.4) \mu\text{F cm}^{-2}$), again most likely due to revealing a significant number of oxygen-containing redox active surface groups. Although a similar affect was seen with the highest-doped electrode G (very high, thin), the capacitance values are abnormally high for both as-received and acid-cycled; $153 (\pm 3)$ to $381 (\pm 8) \mu\text{F cm}^{-2}$. Giant capacitances at heavily doped BDD have been previously observed and attributed to NDC content;¹⁵ however, as the Raman spectrum for electrode G does not indicate significantly high sp^2 content, we speculate that the material may contain cracks and pinholes not visible in FE-SEM³⁸ or boron carbide phases which adversely affect the electrochemical response.³⁹ Unfortunately, the Raman signature of boron carbide is likely to be masked by features associated with BDD.⁴⁰

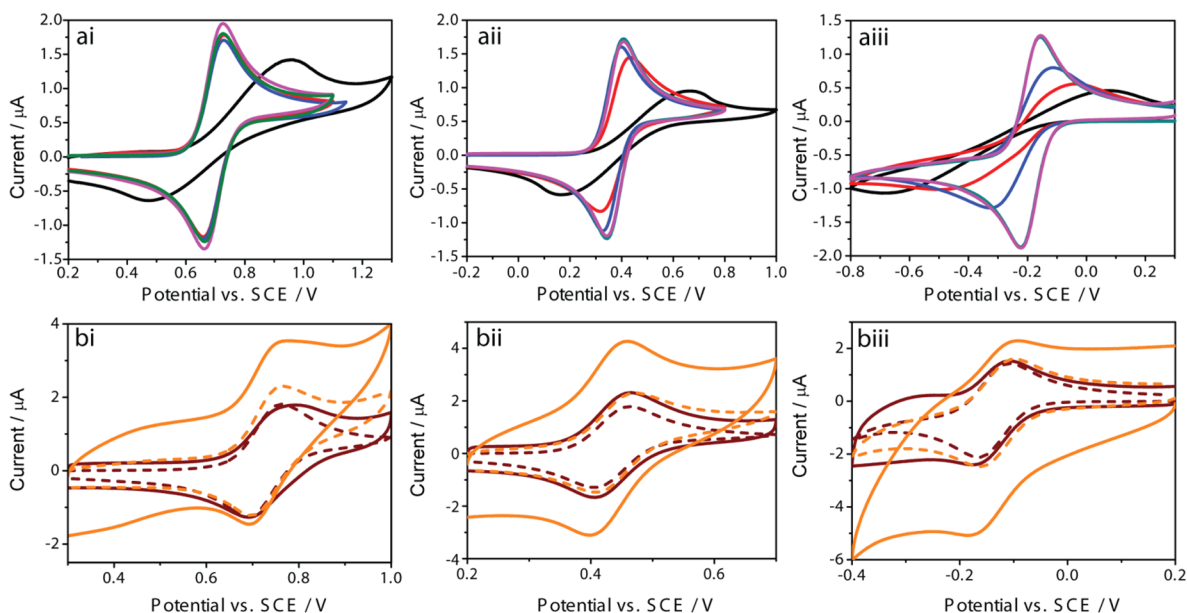


Figure 4. CVs performed with 1 mm diameter disc pBDD (a) electrodes A (black), B (red), C (blue), D (pink), and E (green) and (b) electrodes F (brown) and G (orange), with an as-grown (dashed) or oxygen-terminated (solid) surface, at a scan rate of 0.1 V s^{-1} for (i) the oxidation of 1 mM IrCl_6^{3-} , (ii) the oxidation of 1 mM FcTMA^+ , and (iii) the reduction of $1 \text{ mM Ru(NH}_3)_6^{3+}$ in 0.1 M KNO_3 .

pBDD Outer-Sphere Redox Processes. To assess the performance of the seven pBDD electrodes, the electrochemical CV characteristics were recorded for three outer-sphere redox active species, whose formal potentials, E^0 , cover a wide potential range, all reported with respect to a SCE reference electrode. These include $\text{IrCl}_6^{2-/3-}$ ($E^0 = 0.67 \text{ V}$), $\text{FcTMA}^{+/2+}$ ($E^0 = 0.35 \text{ V}$), and $\text{Ru(NH}_3)_6^{3+/2+}$ ($E^0 = -0.16 \text{ V}$), as shown in Figure 4a (freestanding pBDD) and Figure 4b (thin film pBDD). The peak to peak separations, ΔE_p , for each pBDD electrode are summarized in Table 2.

Table 2. Summary of Electrochemical Characteristics of the Seven Different pBDD Electrodes, All Performed in 0.1 M KNO_3

pBDD electrode	$1 \text{ mM IrCl}_6^{2-/3-}$ ΔE_p (mV)	$1 \text{ mM FcTMA}^{+/2+}$ ΔE_p (mV)	$1 \text{ mM Ru(NH}_3)_6^{3+/2+}$ ΔE_p (mV)
A ($R = 52 \text{ k}\Omega$)	554 (± 9)	589 (± 7)	642 (± 6)
B ($R = 1.1 \text{ k}\Omega$)	80 (± 6)	105 (± 6)	615 (± 8)
C ($R = 180 \Omega$)	69 (± 3)	72 (± 9)	212 (± 9)
D ($R = 0.5 \Omega$)	62 (± 2)	62 (± 3)	68 (± 4)
	$k_{\text{app}}^0 \geq 0.1$	$k_{\text{app}}^0 \geq 0.1$	$k_{\text{app}}^0 = 0.04$
E ($R = 0.4 \Omega$)	61 (± 2)	61 (± 2)	65 (± 2)
	$k_{\text{app}}^0 \geq 0.1$	$k_{\text{app}}^0 \geq 0.1$	$k_{\text{app}}^0 = 0.06$
F; as-received	76 (± 2)	64 (± 3)	66.5 (± 4)
F; O-term	84.5 (± 3)	60.5 (± 2)	55.5 (± 4)
G; as-received	67.5 (± 2)	63.5 (± 2)	66 (± 2)
G; O-term	72.5 (± 3)	60.5 (± 2)	95 (± 5)

For electrodes A (low, fs) to E (high, fs), for the mediators IrCl_6^{3-} , FcTMA^+ , and $\text{Ru(NH}_3)_6^{3+}$, the lowest-doped electrode A shows the largest ΔE_p (and smallest peak currents, i_p), which increase in value, with a corresponding decrease in i_p , as the formal potential of the redox species becomes more negative. This is further exacerbated by increasing the concentration of the redox species (data not shown), reflective of the p-type semiconducting nature of electrode A. A similar trend is seen

for the higher-doped semiconducting electrodes B (low-mid, fs) and C (mid, fs), except the observed ΔE_p values are smaller.

For electrodes D (high, fs) and E (high, fs), the ΔE_p values are very close to reversible for all three redox mediators investigated, irrespective of the potential range. This indicates that these electrodes are doped sufficiently to behave as metal-like electrodes, as even in the negative potential window, where charge depletion effects dominate for semiconducting electrodes there are a sufficient number of charge carriers available to maintain efficient HET. A range of apparent HET rate constants, k_{app}^0 , were simulated and fitted against the experimental CVs. The finite element simulations based on Butler–Volmer HET kinetics are reported in section 4 of the Supporting Information. For the metallic electrodes D (high, fs) and E (high, fs), an ohmic drop term due to the resistance of the diamond material, R_1 , was incorporated into the model, calculated as $R_1 = \rho l/A$, where ρ = diamond sheet resistivity, l = diamond thickness, and A = electrode cross-sectional area. Table 2 shows the best fit k_{app}^0 values for the different redox mediators for electrodes D and E.

From the simulations, we estimate k_{app}^0 values $> 0.1 \text{ cm s}^{-1}$ for IrCl_6^{3-} and FcTMA^+ , with slightly lower values of (D) 0.04 cm s^{-1} and (E) 0.06 cm s^{-1} for $\text{Ru(NH}_3)_6^{3+}$, which may be due to its lower self-exchange rate constant, k_{exch} , of $4 \times 10^3 \text{ M}^{-1} \text{ s}^{-1}$. These values compare favorably to HET-reported rate constants on GC electrodes^{3b,c} and demonstrate that it is possible to produce sufficiently doped diamond electrodes, which, despite having a lower LDOS than a metal electrode, can support fast HET. Moreover, this data shows it is not necessary to employ very high-doping levels, [i.e., $> 10^{21} \text{ B atoms cm}^{-3}$ (> 1 in 100 C atoms replaced with B)], or incorporate NDC to achieve fast HET rates with BDD.⁴¹ Note in the literature, in some cases, highly doped boron electrodes have shown increased catalytic activity over lower doped ones, however Raman indicated a significantly higher NDC content, which is the most likely cause of the observed response.⁴²

The CV data for the thin film metallic electrodes F (high, thin) and G (very high, thin) for both as-received and oxygen-

terminated surfaces are shown in Figure 4b. While comparable, ΔE_p values to electrodes D (high, fs) and E (high, fs) are recorded, the effect of the larger background currents (Figure 3) on the faradaic response is clearly seen, especially after oxygen termination. Hence, we did not attempt to quantify k_{app}^0 for electrodes F and G. For semiconducting electrodes, R_1 does not account for potential dependent interfacial resistance changes due to charge depletion/accumulation effects.⁴³ Therefore, a second potential dependent R_2 term was introduced, as described in section 4 of the Supporting Information.

Hydrogen and Oxygen Termination, Stability, and Surface-Sensitive Processes. To explore the electrochemical response and, more importantly, stability of hydrogen versus oxygen-terminated surfaces, CV measurements were recorded using both lapped, freestanding semiconducting pBDD electrode B (dopant density of 2×10^{18} B atoms cm^{-3}) and metallic pBDD electrode E. The outer sphere redox couple $\text{Ru}(\text{NH}_3)_6^{3+}$ was employed as its formal potential is sufficiently in the band gap region, vide infra, to show very different electrochemical characteristics for the two differently doped electrodes (Figure 4). Electrode E was chosen for these studies, as E shows the optimal characteristics of all “metal-like” electrodes investigated in terms of minimal NDC, widest solvent window and lowest capacitive currents.

Figure 5a shows CVs recorded at hydrogen- (dashed) and oxygen- (alumina polished; solid line) terminated electrodes B

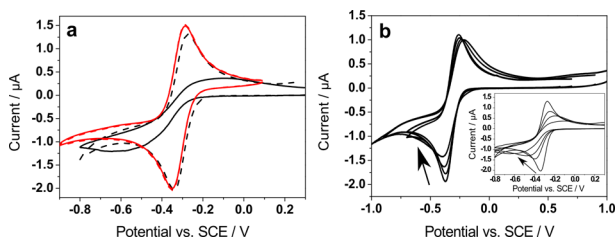


Figure 5. CVs performed with pBDD 1 mm diameter disc electrodes B (black) and E (red) with a freshly hydrogen-terminated surface (dashed line) and acid cleaned oxygen-terminated surface (solid line) at a scan rate of 0.1 V s^{-1} for the reduction of (a) $1 \text{ mM Ru}(\text{NH}_3)_6^{3+}$ in 0.1 M KNO_3 . (b) CVs performed with electrode B for the reduction of $1 \text{ mM Ru}(\text{NH}_3)_6^{3+}$ in 0.1 M KNO_3 , where the potential has been cycled between increasingly extreme potentials of ± 0.6 , ± 0.7 , ± 0.9 , and $\pm 1 \text{ V}$; the electrode was cycled 5 times at each potential range and the first CV is plotted. The inset shows CVs performed with electrode B for the reduction of $1 \text{ mM Ru}(\text{NH}_3)_6^{3+}$ in 0.1 M KNO_3 after subsequent potential windows from 1.5 to -1.5 V in 0.1 M KNO_3 .

(black line) and E (red line). For electrode E (high, fs), ΔE_p is independent of whether the surface is hydrogen- or oxygen-terminated; however, hydrogen-termination of electrode B (low-mid, fs) results in a significant decrease in ΔE_p from 615 mV to 140 mV , suggesting a significant increase in HET. Although hydrogen-termination does not alter the intrinsic bulk resistance of the diamond, it does cause the density of charge carriers to increase, as holes form in an accumulation layer at the diamond surface, decreasing the potential drop across the depletion layer, resulting in the observed increase in HET.⁴⁴

It has been shown that the application of very positive potentials (a few volts) in acidic media is sufficient to almost completely convert from a hydrogen- to an oxygen-terminated surface.⁴⁵ However, it was of interest here to investigate the electrochemical stability of the hydrogen-terminated layer

under potential conditions and less extreme pH conditions more akin to conventional electrochemical measurements, in order to verify whether hydrogen-termination of semiconducting electrodes was a viable route for increasing HET. In order to do this, electrochemical studies focused on hydrogen-terminated semiconducting electrode B with $\text{Ru}(\text{NH}_3)_6^{3+}$ in 0.1 M KNO_3 ($\text{pH} = 6$).

Figure 5b shows the reduction of $1 \text{ mM Ru}(\text{NH}_3)_6^{3+}$ over the potential ranges ± 0.6 , ± 0.7 , ± 0.9 , and $\pm 1 \text{ V}$ versus SCE, where the first CV of five, for each potential range is shown. The first CV recorded is in agreement with the CV data shown in Figure 5a; however, after just five potential cycles, the second CV shown displays a slight decrease in i_p and increase in ΔE_p (154 mV), which is exacerbated with repeated scanning, especially as the potential range is slowly increased by 100 mV each five cycles. This effect was not seen for the oxygen-terminated surface.

This data indicates that the surface termination is slowly being converted from hydrogen to oxygen; an affect which is exacerbated as the potential is increased. Importantly, we show conversion occurs at even relatively mild applied potentials in close to neutral pH conditions, which can lead to possible misinterpretation in HET data, if not accounted for. The inset to Figure 5b shows the effect of running a solvent window between $\pm 1.5 \text{ V}$ in 0.1 M KNO_3 on a freshly hydrogen-terminated electrode B (low-mid, fs). After just three potential cycles, the resulting CV now closely resembles that of the oxygen-terminated surface. Hence, although hydrogen-termination can significantly improve the HET capabilities of a semiconducting BDD electrode, it is not an electrochemically stable surface and even the application of mild potentials will cause deterioration. Unfortunately, re-hydrogen-terminating the surface is nontrivial and can only be done reliably through exposure to hydrogen plasma or through hydrogen dosing.^{44a} This data, and the CV data presented in Figure 4, also highlight that the redox couple $\text{Ru}(\text{NH}_3)_6^{3+}$ is the most appropriate to use when assessing the HET properties of an unknown [B] BDD oxygen-terminated electrode. This is due to its high sensitivity to the electrical properties of pBDD and outer-sphere characteristics.

pBDD Surface Sensitive Redox Processes. Surface sensitive HET processes will also be strongly influenced by the surface termination of the electrode. Studies focused on two differently oxygen-terminated surfaces for electrode E (high, fs) with two different surface sensitive redox couples, $\text{Fe}(\text{CN})_6^{4-/3-}$ and $\text{Fe}^{2+/3+}$.⁴⁷ For highly doped pBDD, HET kinetics of $\text{Fe}(\text{CN})_6^{4-/3-}$ are reported to be slower at oxygen- than hydrogen-terminated pBDD surfaces.^{11b,48} It has been suggested that oxygen functional groups inhibit HET of $\text{Fe}(\text{CN})_6^{4-/3-}$ due to blocking of adsorption sites.^{11b,49} Alternative theories⁵⁰ consider that it is the negative charge on oxygen-containing groups which repel the negatively charged redox species. In contrast, studies by McEvoy have shown mechanical cleaning to mildly improve the kinetics for $\text{Fe}(\text{CN})_6^{4-/3-}$ thought to be due to hydrocarbon contaminant removal.⁵¹ Some forms of anodic pretreatment have also been shown to improve HET kinetics.^{49,52} The differences in the BDD literature also highlight the fact that it is vitally important when measuring HET to carefully assess the material and surface properties so comparative assessments between different group's measurements can be made.

Several methods exist for oxygen termination, including boiling in acid,^{13,17} alumina polishing, exposure to oxygen

plasma,⁵³ photochemical oxidation,^{48c} reaction with oxygen at high temperatures,²¹ and probably the most common anodic polarization.⁵⁴ Here, we use two contrasting procedures, alumina polish, commonly used by researchers as the electrode-cleaning step prior to electrochemical measurement, and anodic polarization in acid. Figure 6ai shows CVs for 1 mM

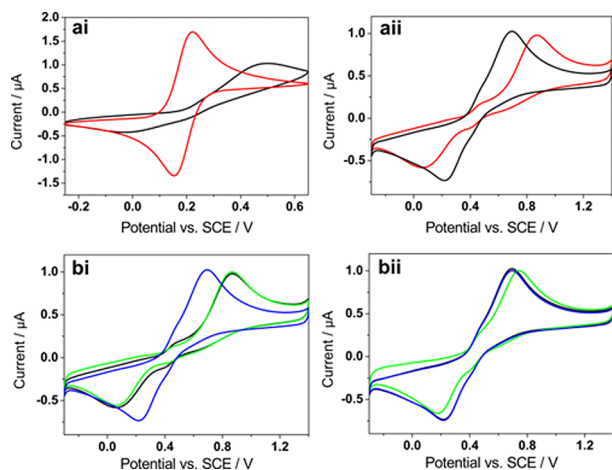


Figure 6. (a) CVs performed with 1 mm diameter disc electrode E after alumina polish (red) and anodic pretreatment (black) for the oxidation of (i) 1 mM Fe(CN)_6^{4-} in 0.1 M KNO_3 and (ii) 1 mM Fe^{2+} in 0.1 M HClO_4 . (b) CVs for the oxidation of 1 mM Fe^{2+} in 0.1 M HClO_4 after 5 s treatment at either -1.5 V (green) or 2 V (blue) for the (i) alumina-polished (black) and (ii) anodically polarized electrode (black).

Fe(CN)_6^{4-} in 0.1 M KNO_3 with electrode E, at a scan rate of 0.1 V s^{-1} oxygen-terminated via alumina polishing (red) and anodic polarization (black) for 60 s at 3 V versus SCE in 0.1 M H_2SO_4 . These are representative of at least $n = 20$ measurements on freshly prepared electrodes.

Alumina polishing electrode E results in a near reversible response for Fe(CN)_6^{4-} electrolysis (ΔE_p of 65 mV). When electrode size has been taken into account and all studies in the literature have been compared, this represents the fastest reported HET kinetics for this couple at an oxygen-terminated, metal-like pBDD electrode. In contrast, after anodic polarization, the effect on the CV behavior is dramatic, with ΔE_p increasing in value from near reversible to 500 mV and the currents falling in magnitude indicative of significantly reduced HET.

To investigate further, XPS was performed on the two oxygen-terminated surfaces. Figure 7 shows typical C1s XPS spectra for (i) alumina polished and (ii) anodically polarized pBDD electrodes recorded at (a) room temperature and after elevation to (b) 300 and (c) 500 °C. A wide XPS survey scan, as shown in section 5 of the Supporting Information, showed no aluminum, indicating the surface had been cleaned of all alumina particles. The data for all spectra was fitted using Lorentzian–Gaussian peaks after a Shirley background subtraction to investigate the chemical environments in which carbon is present at the surface.

For the room temperature alumina-polished surface, spectra (ai), the largest component (peak 1) found at 284.6 eV can be attributed to the $\text{sp}^3 \text{ C-C}$ present in the diamond bulk; all other component peaks are given relative to this one. Higher-binding energies have been associated with carbon in the form of adsorbed hydrocarbons (+0.6 to +0.9 eV) and different forms of oxidation [e.g., alcohol (C-OH) and ether (C-O-C) (+1–2 eV), carbonyl C=O (+2.9–3.8 eV), and carboxyl COOH (+3.7–4.3 eV)].^{51,55} These assignments suggest the presence of C-OH and C-O-C groups (peak 2), as well as C=O groups (peak 3). Peak 6 at lower energies (–1 to –2.1 eV) can be assigned to $\text{sp}^2 \text{ C-C}$, where reconstruction of the diamond surface, especially at the polycrystalline grain boundaries, may give rise to π bonding. Although no evidence of sp^2 was seen in the Raman spectra, XPS is a much more sensitive surface technique.

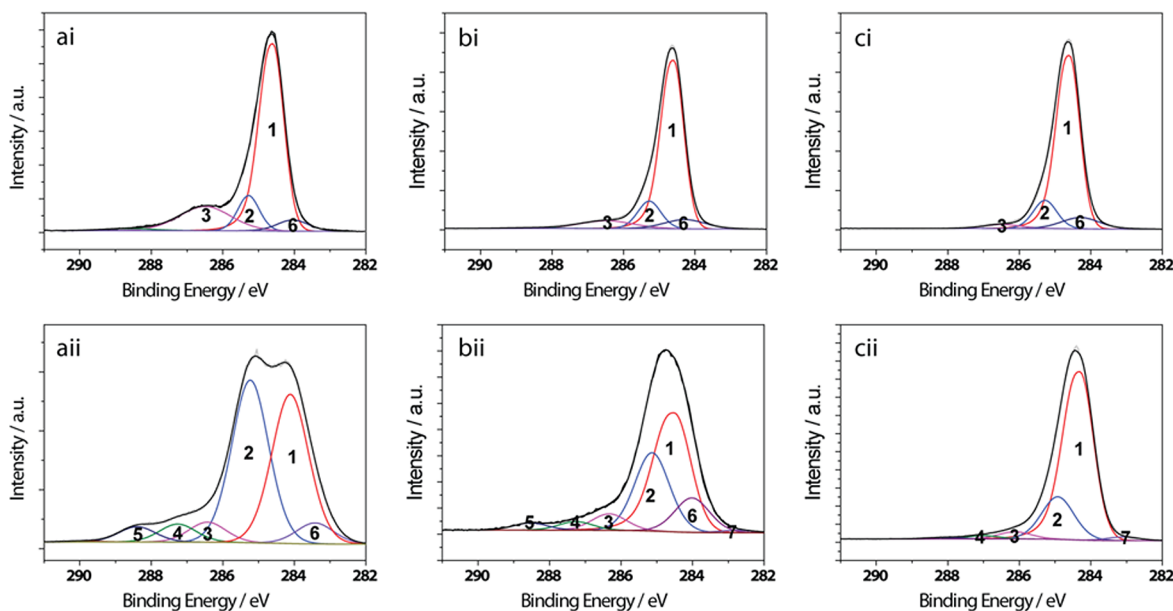


Figure 7. C1s XPS spectra for pBDD electrode E at (a) room temperature and upon heating to (b) 300 °C and (c) 500 °C for an (i) alumina polished and (ii) anodically polarized surface with peak fitting, where the gray line is the experimental data, colored peaks are fittings, and the black is the overall fit.

To gain further insight, XPS was also performed after heating to elevated temperatures, as shown in Figure 7 (panels bi and ci), respectively. Peak 3, associated with ketonic ($\text{C}=\text{O}$) functional groups, decreases significantly after heating to 300 °C (7% of peak 1) and is almost completely removed after heating to 500 °C (3% of peak 1). In contrast, peak 2 (ethers and alcohols) appears stable at these temperatures. This is in agreement with reports which show that $\text{C}=\text{O}$ groups are more weakly bound to the surface than $\text{C}-\text{O}-\text{C}$ groups and are thus more easily removed at lower temperatures (100–400 °C).⁵⁶ Importantly, the XPS spectra after heating to 500 °C resembles that of an in situ annealed single crystal,⁵⁷ indicating the high quality of this electrode material.

These peak assignments can also be applied to the anodically polarized XPS spectra in Figure 7ii, which at room temperature are dramatically different to the alumina-polished surface. The main sp^3 $\text{C}-\text{C}$ peak 1 has shifted slightly to a lower binding energy of 284.2 eV, indicating charging effects or a change in the valence band position. Peak 2 is a much larger component of the $\text{C}1\text{s}$ spectra (107% of peak 1) compared to the alumina polished surface. Increases in peak 2 have previously been observed after anodic treatment but to varying degrees.^{57,58} A significant tail at the higher binding energies (peaks 3–5, spanning +2.2 to +5.4 eV) indicates the presence of highly oxidized carbon functional groups such as COOH and even polycarbonate groups (41% of peak 1).^{55c,59} Upon heating to 300 °C, a decrease in peaks 3–5 (26% of peak 1) is observed, and also peak 2 (64% of peak 1), with further decreases after heating to 500 °C. For this surface, the data suggests that many of the carbon–oxygen groups are only weakly adsorbed to the surface and may even be present in an adsorbed layer. At 500 °C, the surfaces of the two differently prepared electrodes give similar XPS spectra.

Given that we obtain reversible HET for $\text{Fe}(\text{CN})_6^{4-/3-}$ at our alumina polished surface, the concentration of ketonic, ether and alcohol groups on this surface are not sufficient to hinder HET of this mediator. However, as soon as more oxidized groups are introduced (e.g., COOH) (which are also likely to be present for electrodes containing non-negligible NDC) and the concentration of ether and alcohol groups significantly increase, the effect on HET is dramatic, resulting in $\text{Fe}(\text{CN})_6^{4-}$ -surface interactions, which slow down HET. Note, we can rule out any possible electronic factors associated with the material not being sufficiently doped. This data also re-emphasizes that the $\text{Fe}(\text{CN})_6^{4-}$ couple should be treated with caution when being used to assess the HET properties of an electrode.⁶⁰ Finally, simply alumina polishing an anodically treated surface resulted in the attainment of reversible HET for $\text{Fe}(\text{CN})_6^{4-}$.

Further investigations employed the classic inner-sphere redox couple $\text{Fe}^{2+/3+}$. Figure 6aii shows CVs for the oxidation of 1 mM Fe^{2+} in 0.1 M HClO_4 at a scan rate of 0.1 V s^{-1} for alumina polished (red) and anodically polarized (black) electrode E. ΔE_p at the alumina-polished electrode was 803 mV, which decreased to 472 mV upon anodic pretreatment. This increase in HET is likely to be due to the increased presence of functional groups such as carbonyls (including COOH), which favorably mediate HET for this couple.^{3b,46a} Also visible in Figure 6aii is the presence of a small peak, which is unresolved on top of the main CV for both surfaces at 0.47 V (red line) and 0.46 V (black line). Tentatively, we attribute this feature to different rates of HET at different facets (see Figure 1e) on electrode E.

For both surface treatments, it was essential to verify the electrochemical stability of the lapped oxygen-terminated surface, as this is a key requirement in electroanalysis. This was achieved by repeatedly scanning (10 cycles per day) the electrode, in 1 mM Fe^{2+} in 0.1 M HClO_4 , over the potential range from –0.3 V to +1.4 V versus SCE for a week. Both electrodes were found to give very stable responses (ΔE_p values deviated by no greater than ± 12 mV). We found that only by applying more extreme anodic/cathodic potentials was it possible to affect the CV response. For example, as shown in Figure 6bi, when starting with an alumina-polished surface, applying cathodic potentials, –1.5 V for 5 s in 0.1 M HClO_4 (ca. 15 μC passed), had no effect on the CV (ΔE_p of 802 mV); however, 2 V for 5 s in 0.1 M HClO_4 (ca. 15 μC passed) caused ΔE_p to decrease from 803 to 475 mV, as the surface approaches a surface functionality more akin to that obtained with the anodic treatment.

In the case of the anodically polarized surface as shown in Figure 6bii, further anodic polarization, 2 V for 5 s in 0.1 M HClO_4 , gives no change in the response, as expected; however, cathodic polarization, –1.5 V for 5 s in 0.1 M HClO_4 results in a small increase in ΔE_p from 472 to 564 mV. Importantly, for both surfaces, provided the applied potential is not run out too far negative or positive, both forms of surface termination are stable.

CONCLUSIONS

In order to produce pBDD oxygen-terminated electrodes suitable for electroanalysis and exploiting attributes such as low background currents, wide solvent window, high stability, and reproducibility, it is essential that the material properties of the electrode are carefully optimized. First, the material must demonstrate metal-like conductivity. Electrical measurements that demonstrated this were achieved at an average of $[\text{B}] > 10^{20}$ boron atoms cm^{-3} . Although lower $[\text{B}]$ results in larger solvent windows and lower capacitances, the smaller number of charge carriers available at more negative potentials, due to the p-type semiconducting nature of the electrode, result in sluggish HET kinetics for redox couples with formal potentials in the band gap [e.g., $\text{Ru}(\text{NH}_3)_6^{3+}$], which is undesirable. Significantly faster HET for $\text{Ru}(\text{NH}_3)_6^{3+}$ electrolysis at semiconducting electrodes can be obtained by hydrogen-terminating the surface. However, as HET was shown to decrease as the electrode was subjected to successive potential cycles, exacerbated as the potential was increased; the hydrogen-terminated (lapped) surface appears to be electrochemically unstable.

Second, it is essential that no evidence of NDC in either the Raman spectra or the solvent window is observed. In the latter, NDC content is confirmed due to the presence of NDC oxidative currents and/or an oxygen reduction signal in near neutral pH aqueous solutions. In general, the more NDC present, the smaller the solvent window and higher the NDC driven surface currents. As hydrogen-termination can significantly mask NDC-like features in the solvent window, as well as decreasing capacitive currents, it is important to consider this affect when using CV to assess NDC content of as-grown (i.e., H-terminated) electrodes. Note, as we found it impossible to remove NDC completely postgrowth by either diamond polishing or cycling (or boiling) in acid, growth must be carefully controlled to minimize NDC.

Third, it is essential that the $[\text{B}]$ content is optimized. Even though BDD contains a lower density of states than a metal, it

is not necessary to use extreme doping levels (e.g., $> 1 \times 10^{21}$ B atoms cm^{-3}), as increased [B] results in slightly narrower solvent windows, higher capacitance, and can increase the likelihood of NDC incorporation. We found oxygen-terminated pBDD electrodes with an average [B] $\sim 3 \times 10^{20}$ boron atoms cm^{-3} (negligible NDC content), recorded the lowest capacitive currents ($\sim 6 \mu\text{F cm}^{-2}$), widest solvent windows, and achieved fast (reversible) HET for a wide range of outer sphere redox couples, on the experimental timescale provided by a 1 mm diameter electrode scanned at 100 mV s^{-1} .

For the surface-sensitive redox couples, $\text{Fe}(\text{CN})_6^{4-/3-}$ and $\text{Fe}^{2+/3+}$, it is possible to drastically influence HET simply by changing the method of oxygen termination. In particular, for the optimal electrode material employed, alumina polishing of the lapped surface promoted near reversible HET for $\text{Fe}(\text{CN})_6^{4-/3-}$, the fastest reported HET for this couple to date at an oxygen-terminated pBDD electrode. In contrast, anodic polarization resulted in a significant reduction in HET. Less dramatic effects were seen with the redox couple $\text{Fe}^{2+/3+}$, although oxidation of Fe^{2+} was favored on the anodically polarized surface. XPS analysis suggested a higher prevalence of oxygen functional groups, such as carbonyl and carboxyl groups on the anodically polarized surface, and increased levels of ether and alcohol groups, thought to be responsible for the significant decrease in HET for $\text{Fe}(\text{CN})_6^{4-}$, and slightly increased HET for Fe^{2+} . Temperature-dependent XPS studies revealed the alumina cleaned XPS surface to be high quality, containing only monolayer oxygen functionalities. Most importantly, for both methods of oxygen termination, the CV responses for (e.g., $\text{Fe}^{3+/2+}$) were found to be stable over repetitive cycles, over a week of testing.

■ ASSOCIATED CONTENT

■ Supporting Information

Preparation and cleaning procedures for thin film electrodes F and G, Raman Mapping of sp^2 and sp^3 carbon in electrodes D and E, solvent windows for electrodes D, E, Pt, and GC in 0.1 M KNO_3 , finite element simulations for metallic and semiconducting BDD electrodes, and XPS survey spectrum of electrode E. This material is available free of charge via the Internet at <http://pubs.acs.org>.

■ AUTHOR INFORMATION

Corresponding Author

*E-mail: j.macpherson@warwick.ac.uk. Tel: 0247673886.

Notes

The authors declare no competing financial interest.

■ ACKNOWLEDGMENTS

J.I. and R.C. acknowledge support from the EPSRC Analytical Fund and EPSRC iCASE, respectively. We thank Dr. Jim Butler (NRL) and E6 for provision of the samples. We are grateful to Dr. Andy Evans (Department of Physics, Aberystwyth University) and Dr. Gruff Williams (E6) for helpful discussions on XPS interpretation and Dr. Marc Walker (Department of Physics, University of Warwick) for recording the XPS data. Finally, we thank Advantage West Midlands and the European Regional Development Fund for providing some of the equipment used in this research.

■ REFERENCES

- (1) (a) Gilmartin, M. A. T.; Hart, J. P. *Analyst* **1995**, *120*, 1029–1045. (b) Compton, R. G.; Foord, J. S.; Marken, F. *Electroanalysis* **2003**, *15*, 1349–1363.
- (2) (a) Huang, X.; Zeng, Z.; Fan, Z.; Liu, J.; Zhang, H. *Adv. Mater.* **2012**, *24*, 5979–6004. (b) Brownson, D. A. C.; Kampouris, D. K.; Banks, C. E. *Chem. Soc. Rev.* **2012**, *41*, 6944–6976. (c) Sharma, S.; Pollet, B. G. *J. Power Sources* **2012**, *208*, 96–119.
- (3) (a) Engstrom, R. C. *Anal. Chem.* **1982**, *54*, 2310–2314. (b) Chen, P. H.; Fryling, M. A.; McCreery, R. L. *Anal. Chem.* **1995**, *67*, 3115–3122. (c) Cline, K. K.; McDermott, M. T.; McCreery, R. L. *J. Phys. Chem.* **1994**, *98*, 5314–5319. (d) Dumitrescu, I.; Unwin, P. R.; Macpherson, J. V. *Chem. Commun. (Cambridge, U.K.)* **2009**, 6886–6901.
- (4) (a) Kraft, A. *Int. J. Electrochem. Sci.* **2007**, *2*, 355–385. (b) Luong, J. H. T.; Male, K. B.; Glennon, J. D. *Analyst* **2010**, *135*, 3008–3008. (c) Liu, Y.; Wipf, D. O.; Henry, C. S. *Analyst* **2001**, *126*, 1248–1251.
- (5) (a) Alehashem, S.; Chambers, F.; Strojek, J. W.; Swain, G. M.; Ramesham, R. *Anal. Chem.* **1995**, *67*, 2812–2821. (b) Vinokur, N.; Miller, B.; Avyigal, Y.; Kalish, R. *J. Electrochem. Soc.* **1996**, *143*, L238–L240. (c) Swain, G. M.; Ramesham, R. *Anal. Chem.* **1993**, *65*, 345–351.
- (6) (a) Pleskov, Y. V. *Russ. J. Electrochem.* **2002**, *38*, 1275–1291. (b) Xu, J.; Granger, M. C.; Chen, Q. Y.; Strojek, J. W.; Lister, T. E.; Swain, G. M. *Anal. Chem.* **1997**, *69*, S91A–S97A. (c) Swain, G. M. *Adv. Mater.* **1994**, *6*, 388–392.
- (7) (a) Lagrange, J. P.; Deneuille, A.; Gheeraert, E. *Diamond Relat. Mater.* **1998**, *7*, 1390–1393. (b) Gheeraert, E.; Deneuille, A.; Mambou, J. *Diamond Relat. Mater.* **1998**, *7*, 1509–1512. (c) Inushima, T.; Matsushita, T.; Ohya, S.; Shiomi, H. *Diamond Relat. Mater.* **2000**, *9*, 1066–1070. (d) Shiomi, H.; Nishibayashi, Y.; Fujimori, N. *Jpn. J. Appl. Phys. Part 1* **1991**, *30*, 1363–1366. (e) Nishimura, K.; Das, K.; Glass, J. T. *J. Appl. Phys.* **1991**, *69*, 3142–3148. (f) Tenne, R.; Patel, K.; Hashimoto, K.; Fujishima, A. *J. Electroanal. Chem.* **1993**, *347*, 409–415.
- (8) Issaoui, R.; Achard, J.; Silva, F.; Tallaie, A.; Tardieu, A.; Gicquel, A.; Pinault, M. A.; Jomard, F. *Appl. Phys. Lett.* **2010**, *97*, 182101–182103.
- (9) Charles, S. J.; Steeds, J. W.; Evans, D. J. F.; Butler, J. E. *Mater. Lett.* **2003**, *57*, 3690–3693.
- (10) (a) Martin, H. B.; Argoitia, A.; Landau, U.; Anderson, A. B.; Angus, J. C. *J. Electrochem. Soc.* **1996**, *143*, L133–L136. (b) Trouillon, R.; O'Hare, D. *Electrochim. Acta* **2010**, *55*, 6586–6595. (c) Bennett, J. A.; Wang, J. A.; Show, Y.; Swain, G. M. *J. Electrochem. Soc.* **2004**, *151*, E306–E313.
- (11) (a) Granger, M. C.; Witek, M.; Xu, J. S.; Wang, J.; Hupert, M.; Hanks, A.; Koppang, M. D.; Butler, J. E.; Lucazeau, G.; Mermoux, M.; Strojek, J. W.; Swain, G. M. *Anal. Chem.* **2000**, *72*, 3793–3804. (b) Granger, M. C.; Swain, G. M. *J. Electrochem. Soc.* **1999**, *146*, 4551–4558. (c) Fischer, A. E.; Show, Y.; Swain, G. M. *Anal. Chem.* **2004**, *76*, 2553–2560.
- (12) Schäfer, H. J.; Schneider, R. *Tetrahedron* **1991**, *47*, 715–724.
- (13) Liu, F. B.; Wang, J. D.; Liu, B.; Li, X. M.; Chen, D. R. *Diamond Relat. Mater.* **2007**, *16*, 454–460.
- (14) (a) Salazar-Banda, G. R.; Andrade, L. S.; Nascente, P. A. P.; Pizani, P. S.; Rocha, R. C.; Avaca, L. A. *Electrochim. Acta* **2006**, *51*, 4612–4619. (b) Godfried, H. P.; Coe, S. E.; Hall, C. E.; Pickles, C. S. J.; Sussmann, R. S.; Tang, X.; van der Voorden, W. K. L. In *Use of CVD Diamond in High-Power CO₂ Lasers and Laser Diode Arrays*; SPIE: Bellingham, WA, 2000.
- (15) Watanabe, T.; Shimizu, T. K.; Tateyama, Y.; Kim, Y.; Kawai, M.; Einaga, Y. *Diamond Relat. Mater.* **2010**, *19*, 772–777.
- (16) Prado, C.; Wilkins, S. J.; Grundler, P.; Marken, F.; Compton, R. G. *Electroanalysis* **2003**, *15*, 1011–1016.
- (17) Bachmann, P. K.; Leers, D.; Lydtin, H. *Diamond Relat. Mater.* **1991**, *1*, 1–12.
- (18) Olivia, H.; Sarada, B. V.; Shin, D.; Rao, T. N.; Fujishima, A. *Analyst* **2002**, *127*, 1572–1575.

- (19) Tsai, Y. C.; Coles, B. A.; Holt, K.; Foord, J. S.; Marken, F.; Compton, R. G. *Electroanalysis* **2001**, *13*, 831–835.
- (20) Hutton, L.; Newton, M. E.; Unwin, P. R.; Macpherson, J. V. *Anal. Chem.* **2009**, *81*, 1023–1032.
- (21) Ostrovskaya, L.; Perevertailo, V.; Ralchenko, V.; Dementjev, A.; Loginova, O. *Diamond Relat. Mater.* **2002**, *11*, 845–850.
- (22) Zuo, S. S.; Yaran, M. K.; Grotjohn, T. A.; Reinhard, D. K.; Asmussen, J. *Diamond Relat. Mater.* **2008**, *17*, 300–305.
- (23) Balmer, R. S.; Brandon, J. R.; Clewes, S. L.; Dhillon, H. K.; Dodson, J. M.; Friel, I.; Inglis, P. N.; Madgwick, T. D.; Markham, M. L.; Mollart, T. P.; Perkins, N.; Scarsbrook, G. A.; Twitchen, D. J.; Whitehead, A. J.; Wilman, J. J.; Woollard, S. M. *J. Phys.: Condens. Matter* **2009**, *21*, 364221.
- (24) Wilson, N. R.; Clewes, S. L.; Newton, M. E.; Unwin, P. R.; Macpherson, J. V. *J. Phys. Chem. B* **2006**, *110*, 5639–5646.
- (25) Bernard, M. *Diamond Relat. Mater.* **2004**, *13*, 282–286.
- (26) Locher, R.; Wagner, J.; Fuchs, F.; Maier, M.; Gonon, P.; Koidl, P. *Diamond Relat. Mater.* **1995**, *4*, 678–683.
- (27) Levy-Clement, C.; Ndao, N. A.; Katty, A.; Bernard, M.; Deneuville, A.; Comninellis, C.; Fujishima, A. *Diamond Relat. Mater.* **2003**, *12*, 606–612.
- (28) (a) Locher, R.; Wagner, J.; Fuchs, F.; Wild, C.; Hiesinger, P.; Gonon, P.; Koidl, P. *Mater. Sci. Eng., B* **1995**, *29*, 211–215. (b) Ushizawa, K.; Watanabe, K.; Ando, T.; Sakaguchi, I.; Nishitani-Gamo, M.; Sato, Y.; Kanda, H. *Diamond Relat. Mater.* **1998**, *7*, 1719–1722. (c) Gheeraert, E.; Deneuville, A.; Mambou, J. *Carbon* **1999**, *37*, 107–111.
- (29) Levy-Clement, C.; Zenia, F.; Ndao, N. A.; Deneuville, A. *New Diamond Front. Carbon Technol.* **1999**, *9*, 189–206.
- (30) (a) Mermoux, M.; Marcus, B.; Swain, G. M.; Butler, J. E. *J. Phys. Chem. B* **2002**, *106*, 10816–10827. (b) Praver, S.; Nemanich, R. J. *Philos. Trans. R. Soc., A* **2004**, *362*, 2537–2565.
- (31) (a) Correia, A. N.; Machado, S. A. S. *Electrochim. Acta* **1998**, *43*, 367–373. (b) Damjanovic, A.; Dey, A.; Bockris, J. O. M. *Electrochim. Acta* **1966**, *11*, 791–814.
- (32) Thomas, R. E.; Rudder, R. A.; Markunas, R. J. *J. Vac. Sci. Technol., A* **1992**, *10*, 2451–2457.
- (33) (a) Yeager, E. *Electrochim. Acta* **1984**, *29*, 1527–1537. (b) Hossain, M. S.; Tryk, D.; Yeager, E. *Electrochim. Acta* **1989**, *34*, 1733–1737.
- (34) Martin, H. B.; Argoitia, A.; Angus, J. C.; Landau, U. *J. Electrochem. Soc.* **1999**, *146*, 2959–2964.
- (35) Yano, T.; Tryk, D. A.; Hashimoto, K.; Fujishima, A. *J. Electrochem. Soc.* **1998**, *145*, 1870–1876.
- (36) Živcová, Z. V.; Frank, O.; Petrák, V.; Tarábková, H.; Vacík, J.; Nesládek, M.; Kavan, L. *Electrochim. Acta* **2013**, *87*, 518–525.
- (37) Patten, H. V.; Meadows, K. E.; Hutton, L. A.; Iacobini, J. G.; Battistel, D.; McKelvey, K.; Colburn, A. W.; Newton, M. E.; Macpherson, J. V.; Unwin, P. R. *Angew. Chem., Int. Ed.* **2012**, *51*, 7002–7006.
- (38) Chaplin, B. P.; Hubler, D. K.; Farrell, J. *Electrochim. Acta* **2013**, *89*, 122–131.
- (39) Hartley, A. M.; Axelrod, H. D. *J. Electroanal. Chem. Interfacial Electrochem.* **1968**, *18*, 115–121.
- (40) Tallant, D. R.; Aselage, T. L.; Campbell, A. N.; Emin, D. *Phys. Rev. B* **1989**, *40*, 5649–5656.
- (41) Fierro, S.; Abe, K.; Comninellis, C.; Einaga, Y. *J. Electrochem. Soc.* **2011**, *158*, F183–F189.
- (42) Feng, Y.; Lv, J.; Liu, J.; Gao, N.; Peng, H.; Chen, Y. *Appl. Surf. Sci.* **2011**, *257*, 7–7.
- (43) Gerischer, H. *Physical Chemistry, An Advanced Treatise*; Eyring, H.; Academic: New York, 1970.
- (44) (a) Kawarada, H. *Surf. Sci. Rep.* **1996**, *26*, 205–259. (b) Vassal, N.; Salmon, E.; Fauvarque, J. F. *J. Electrochem. Soc.* **1999**, *146*, 20–26. (c) Ristein, J. *Appl. Phys. A: Mater. Sci. Process.* **2006**, *82*, 377–384.
- (45) Hoffmann, R.; Obloh, H.; Tokuda, N.; Yang, N.; Nebel, C. E. *Langmuir* **2012**, *28*, 47–50.
- (46) (a) Shakkhivel, P.; Chen, S.-M. *Biosens. Bioelectron.* **2007**, *22*, 1680–1687. (b) Pihel, K.; Walker, Q. D.; Wightman, R. M. *Anal. Chem.* **1996**, *68*, 2084–2089.
- (47) Ohnishi, K.; Einaga, Y.; Notsu, H.; Terashima, C.; Rao, T. N.; Park, S. G.; Fujishima, A. *Electrochem. Solid-State Lett.* **2002**, *5*, D1–D3.
- (48) (a) Marken, F.; Paddon, C. A.; Asogan, D. *Electrochem. Commun.* **2002**, *4*, 62–66. (b) Actis, P.; Denoyelle, A.; Boukherroub, R.; Szunerits, S. *Electrochem. Commun.* **2008**, *10*, 402–406. (c) Boukherroub, R.; Wallart, X.; Szunerits, S.; Marcus, B.; Bouvier, P.; Mermoux, M. *Electrochem. Commun.* **2005**, *7*, 937–940.
- (49) El Tall, O.; Jaffrezic-Renault, N.; Sigaud, M.; Vittori, O. *Electroanalysis* **2007**, *19*, 1152–1159.
- (50) Yagi, I.; Notsu, H.; Kondo, T.; Tryk, D. A.; Fujishima, A. *J. Electroanal. Chem.* **1999**, *473*, 173–178.
- (51) McEvoy, J. P.; Foord, J. S. *Electrochim. Acta* **2005**, *50*, 2933–2941.
- (52) Prado, C.; Wilkins, S. J.; Marken, F.; Compton, R. G. *Electroanalysis* **2002**, *14*, 262–272.
- (53) Owen, H. S. H. a. B. B. *The Physical Chemistry of Electrolytic Solutions*; Reinhold: New York, 1958.
- (54) Werner, M.; Job, R.; Zaitzev, A.; Fahrner, W. R.; Seifert, W.; Johnston, C.; Chalker, P. R. *Phys. Status Solidi A* **1996**, *154*, 385–393.
- (55) (a) Girard, H. A.; Simon, N.; Ballutaud, D.; de La Rochefoucauld, E.; Etcheberry, A. *Diamond Relat. Mater.* **2007**, *16*, 888–891. (b) Ghodbane, S.; Ballutaud, D.; Omnes, F.; Agnes, C. *Diamond Relat. Mater.* **2010**, *19*, 630–636. (c) Ballutaud, D.; Simon, N.; Girard, H.; Rzepka, E.; Bouchet-Fabre, B. *Diamond Relat. Mater.* **2006**, *15*, 716–719. (d) Graupner, R.; Maier, F.; Ristein, J.; Ley, L.; Jung, C. *Phys. Rev. B* **1998**, *57*, 12397–12409.
- (56) Field, J. E. *The Properties of Natural and Synthetic Diamond*; Academic Press Limited: London, 1992.
- (57) Denisenko, A.; Pietzka, C.; Romanyuk, A.; El-Hajj, H.; Kohn, E. *J. Appl. Phys.* **2008**, *103*, 014904–014908.
- (58) Goeting, C. H.; Marken, F.; Gutiérrez-Sosa, A.; Compton, R. G.; Foord, J. S. *Diamond Relat. Mater.* **2000**, *9*, 390–396.
- (59) Girard, H. A.; Simon, N.; Ballutaud, D.; Etcheberry, A. C. R. *Chim.* **2008**, *11*, 1010–1015.
- (60) Patel, A. N.; Collignon, M. G.; O’Connell, M. A.; Hung, W. O. Y.; McKelvey, K.; Macpherson, J. V.; Unwin, P. R. *J. Am. Chem. Soc.* **2012**, *134*, 20117–20130.